

Stochastic Rainfall Downscaling of Climate Models

*Original*

Stochastic Rainfall Downscaling of Climate Models / D'Onofrio, D.; Palazzi, E.; von Hardenberg, J.; Provenzale, A.; Calmanti, S.. - In: JOURNAL OF HYDROMETEOROLOGY. - ISSN 1525-755X. - 15:2(2014), pp. 830-843. [10.1175/JHM-D-13-096.1]

*Availability:*

This version is available at: 11583/2815002 since: 2020-04-22T14:10:42Z

*Publisher:*

AMER METEOROLOGICAL SOC

*Published*

DOI:10.1175/JHM-D-13-096.1

*Terms of use:*

This article is made available under terms and conditions as specified in the corresponding bibliographic description in the repository

*Publisher copyright*

(Article begins on next page)

## Stochastic Rainfall Downscaling of Climate Models

D. D'ONOFRIO

*University of Turin, and ISAC-CNR, Turin, Italy*

E. PALAZZI, J. VON HARDENBERG, AND A. PROVENZALE

*ISAC-CNR, Turin, Italy*

S. CALMANTI

*ENEA, UTMEA-CLIM, Rome, Italy*

(Manuscript received 26 May 2013, in final form 4 November 2013)

### ABSTRACT

Precipitation extremes and small-scale variability are essential drivers in many climate change impact studies. However, the spatial resolution currently achieved by global climate models (GCMs) and regional climate models (RCMs) is still insufficient to correctly identify the fine structure of precipitation intensity fields. In the absence of a proper physically based representation, this scale gap can be at least temporarily bridged by adopting a stochastic rainfall downscaling technique. In this work, a precipitation downscaling chain is introduced where the global 40-yr ECMWF Re-Analysis (ERA-40) (at about 120-km resolution) is dynamically downscaled using the Protheus RCM at 30-km resolution. The RCM precipitation is then further downscaled using a stochastic downscaling technique, the Rainfall Filtered Autoregressive Model (RainFARM), which has been extended for application to long climate simulations. The application of the stochastic downscaling technique directly to the larger-scale reanalysis field at about 120-km resolution is also discussed. To assess the ability of this approach in reproducing the main statistical properties of precipitation, the downscaled model results are compared with the precipitation data provided by a dense network of 122 rain gauges in northwestern Italy, in the time period from 1958 to 2001. The high-resolution precipitation fields obtained by stochastically downsampling the RCM outputs reproduce well the seasonality and amplitude distribution of the observed precipitation during most of the year, including extreme events and variance. In addition, the RainFARM outputs compare more favorably to observations when the procedure is applied to the RCM output rather than to the global reanalyses, highlighting the added value of reaching high enough resolution with a dynamical model.

### 1. Introduction

Estimating the expected impact of climate change on hydrometeorological risk, ecosystem functioning, permafrost thawing, snow and glacier melt, and water availability requires precipitation scenarios with high spatial and temporal resolution (Giorgi 2006; Wilby and Fowler 2010). However, current global climate models (GCMs) have spatial resolutions that are usually no higher than 70–120 km (Washington and Parkinson 2005; Solomon et al. 2007). The current trend of increasing the resolution

of GCMs is limited by the enormous computational and storage resources required, the limits of the physical approximations in the models (e.g., hydrostaticity) and the need for retuning the model parameterizations whenever the resolution is increased.

Another approach to achieve higher resolutions is based on the concept of dynamical downscaling, by nesting regional climate models (RCMs) into GCMs (Giorgi 1990; Castro et al. 2005; Giorgi 2006). Recent studies (Paeth and Diederich 2011; Guyennon et al. 2013) suggest, for example, that the production of high-resolution and long-term scenarios is improved by including RCMs as an intermediate step in the downscaling chain. Nonetheless, most regional climate models achieve resolutions that are currently no higher than 20–50 km

---

Corresponding author address: D. D'Onofrio, ISAC-CNR, corso Fiume 4, Torino 10133, Italy.  
E-mail: d.donofrio@isac.cnr.it

(Flaounas et al. 2012), which are still too coarse for hydrological applications and impact studies at the basin scale (Sorooshian et al. 2008). The use of high-resolution nonhydrostatic models, originally developed for meteorological applications (Michalakes et al. 2004), would allow us to reach significantly finer resolutions. However, this approach is still in its infancy for climatic applications and the computational effort required is rather formidable.

In past years, various techniques have been developed to bridge the scale gap between climate change scenarios obtained from regional climate models and the small scales needed for impact studies. An effective approach is provided by statistical and stochastic downscaling techniques. Statistical downscaling maps large-scale deterministic predictors for precipitation at small scales (Maraun et al. 2010; Chiew et al. 2010), to produce realizations of the expected small-scale rainfall field. Stochastic rainfall downscaling (Ferraris et al. 2003a,b) aims at generating synthetic spatiotemporal precipitation fields whose statistical properties are consistent with the small-scale statistics of observed precipitation, based only on knowledge of the large-scale precipitation field. This latter approach has been developed to estimate flood risk in small catchments on meteorological time scales (a few days), and its application in a climatological framework is still largely unexplored. Stochastic downscaling also has the potential for estimating uncertainties in rainfall scenarios, by generating large ensembles of synthetic small-scale precipitation fields that can be compared with measured data (Brussolo et al. 2008). Clearly, stochastic downscaling is not a substitute for physically based models, but it is a way to introduce rainfall variability at scales not resolved by physical models.

In this paper we discuss the results of the application of a robust stochastic downscaling procedure [Rainfall Filtered Autoregressive Model (RainFARM); Rebora et al. 2006b], originally devised for spatiotemporal rainfall downscaling of meteorological predictions, to the output of a state-of-the-art regional climate model (Protheus; Artale et al. 2010; Gualdi et al. 2013) and to the global 40-yr European Centre for Medium-Range Weather Forecasts (ECMWF) Re-Analysis (ERA-40) (the large-scale driver of the Protheus RCM). In order to apply stochastic downscaling to precipitation fields on climatic time scales, we were required to optimize the performance of the downscaling procedure on long time spans. We tested the performance of this approach by comparing the downscaled model outputs with the precipitation data recorded by a dense network of individual rain gauges in the Piedmont and Valle d'Aosta regions, northwestern Italy.

The rest of the paper is organized as follows. Section 2 describes the rain gauge dataset, the Protheus RCM outputs, and ERA-40. We describe the RainFARM

procedure in section 3, discussing the extension that makes it suitable for spatial downscaling of climate models. In section 4, we compare the precipitation climatology obtained from the RCM with the observations, upscaled to the model resolution. In section 5, we show the results of the application of the RainFARM stochastic downscaling procedure to the Protheus model and analyze the resulting precipitation statistics. The results are compared with the direct downscaling of the ERA-40 fields. Discussion and conclusions are reported in the last section.

## 2. Observational data, model outputs, and reanalyses

### a. The observational network

We use daily cumulated precipitation measured by a network of 122 rain gauges located in the Piedmont and Valle d'Aosta regions, northwestern Italy, and managed by the Regional Environmental Protection Agency (ARPA) of Piedmont. The data considered here refer to the period 1958–2001, during which a large number of measuring stations were active. After 2001, the stations were gradually dismissed and substituted with a new and denser network of automatic stations, losing continuity in the individual precipitation records. The data considered here are the same as in Ciccarelli et al. (2008) (to which we refer the reader for details), which were checked for quality and internal consistency, assuring that periods of no station activity were not accounted as periods of no precipitation and by marking outliers and erroneous or suspicious data as missing. The stations are located at different altitudes, ranging from 127 to 2526 m above mean sea level, with resolution ranging from 0.1 (for most stations) to 1 mm day<sup>-1</sup>.

### b. The Protheus system

The Protheus system is an atmosphere–ocean coupled regional climate model for the Mediterranean area (Artale et al. 2010). It is composed by the Regional Climate Model, version 3 (RegCM3), for the atmospheric component (Giorgi et al. 1993a,b) and by a regional configuration of the Massachusetts Institute of Technology General Circulation Model (MITgcm) for the oceanic component (Marshall et al. 1997a,b). The two models are coupled by the Ocean Atmosphere Sea Ice Soil (OASIS3) software, through which coupling fields are exchanged every 6 h. The RegCM3 and MITgcm configurations employed in this study are the same as described in Artale et al. (2010). RegCM3 has a uniform grid spacing of about 30 km, and the spatial domain, which covers the entire Mediterranean, is centered at 41°N and 15°E, with 160 grid points in the meridional direction,

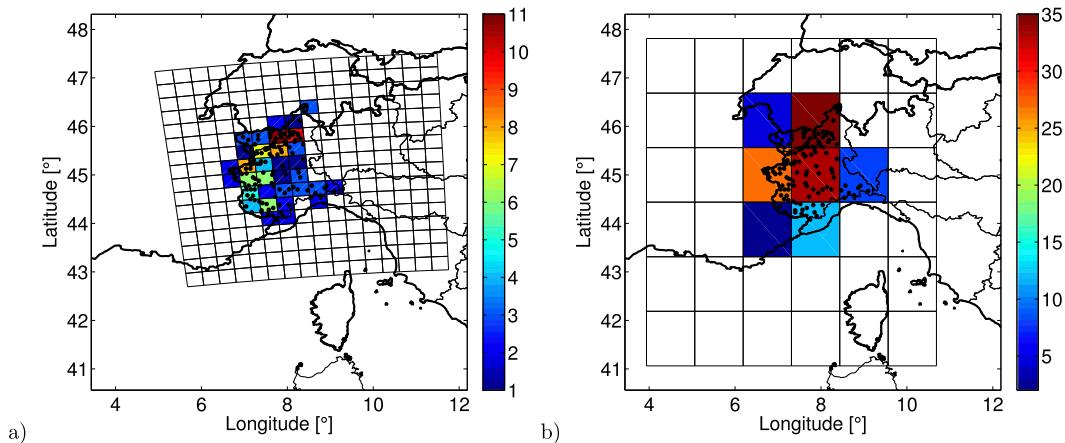


FIG. 1. Numerical grids for (a) the Protheus model and (b) ERA-40. The locations of rain gauges are shown by black dots. Grid elements (pixels) are colored according to the total number of stations they contain.

150 grid points in the zonal direction and 18  $\sigma$  levels in the vertical direction. MITgcm has a spatial resolution of  $1/8^\circ \times 1/8^\circ$ , which corresponds to a nonuniform resolution of  $14 \text{ km} \times (9\text{--}12) \text{ km}$ , the finest resolution being reached in the northern part of the domain. ERA-40 (Uppala et al. 2005) (described below) constitutes the large-scale driver of the Protheus RCM runs considered here, and provides the lateral boundary conditions to RegCM3 every 6 h. The model performance is comparable with that of other state-of-the-art RCMs (Dubois et al. 2012). In particular Dell'Aquila et al. (2012) illustrate how RCMs are able to reconstruct subregional patterns of climate variability and change, which may be missing in coarse-resolution regional drivers.

In this study, we consider daily cumulated precipitation data from the Protheus system for the time period 1958–2001, when observations are available for comparison. The study area is a subdomain of the whole modeling domain, and it ranges from  $42.8^\circ$  to  $47.4^\circ\text{N}$  and from  $5.1^\circ$  to  $11.5^\circ\text{E}$ , containing  $16 \times 16$  pixels.

In the following, all comparisons between model outputs and observations consider only the model pixels containing one or more rain gauge stations. The model pixels that do not contain rain gauges are excluded from the analysis. With this choice, the total number of model pixels actually used for the analysis is 33. Figure 1a shows the model grid and the location of the rain gauges considered in this study (black dots), while the color code refers to the number of stations per model pixel, ranging from a minimum of 1 to a maximum of 11 rain gauges per pixel.

### c. ERA-40

We consider daily cumulated precipitation estimates obtained from ERA-40 (Uppala et al. 2005), spanning the period 1958–2001 and focusing on the region

( $41.0625^\circ\text{--}47.8125^\circ\text{N}$ ,  $3.9375^\circ\text{--}10.6875^\circ\text{E}$ ), which contains  $6 \times 6$  ERA-40 pixels and almost entirely the selected area of the Protheus domain. The available spatial resolution of this product is  $1.125^\circ$ , corresponding in our case to about  $\sim 125$  and  $\sim 88 \text{ km}$  in the latitudinal and longitudinal directions, respectively. Only 7 out of the 36 ERA-40 pixels contain rain gauges, ranging from 11 to 35 rain gauges per pixel. In the following, only these pixels have been used for the comparison between ERA-40 and the observations. The model grid is compared with the position of the measurement stations in Fig. 1b.

It is worth recalling that variables such as temperature are directly assimilated into the reanalysis system, while precipitation is a forecast parameter produced by the model without assimilation. For this reason, significant differences can occur between the precipitation in the reanalysis and the observations, owing to difficulties of large-scale models to account for all of the physical mechanisms affecting the hydrologic cycle, particularly in areas with complex orography (see, e.g., Palazzi et al. 2013).

## 3. The RainFARM procedure

RainFARM (Rebora et al. 2006a,b) is a stochastic downscaling procedure based on the nonlinear transformation of a linearly correlated stochastic field, generated by small-scale extrapolation of the Fourier spectrum of a large-scale field produced by a model or by a reanalysis. Applications of the RainFARM approach include the analysis of the sensitivity of a distributed hydrological model to the variability of the spatiotemporal distribution of rainfall (Gabellani et al. 2007), the estimate of uncertainty in flood predictions (Rebora et al. 2006a), the assessment of the main uncertainty sources in ensemble precipitation forecasts (von Hardenberg et al. 2007), and

the quantification of sampling errors for the verification of meteorological forecasts against rain gauge observations (Brussolo et al. 2008). A comparison between stochastic downscaling of large-scale precipitation fields provided by ECMWF reanalyses, using the RainFARM procedure, and dynamical downscaling with a regional model has revealed comparable probabilistic skills (Brussolo et al. 2009).

The original RainFARM technique was developed for the spatiotemporal downscaling of individual precipitation events on meteorological time scales. Studies of climate change impacts require to downscale precipitation scenarios on long time periods, which include a large number of individual rainfall events with potentially different spectral properties. In addition, the standard temporal resolution of the outputs of state-of-the-art RCMs (on the order of 3 or 6 h in many cases) is often adequate for impact studies. These two characteristics suggest the application of a purely spatial downscaling technique. Along these lines, we introduce a variant of the RainFARM procedure, described below, which is suitable for accurate spatial downscaling. For a description of the original RainFARM procedure, see Reborá et al. (2006b).

In the present variant of RainFARM, a temporal sequence of model-generated (or reanalysis) large-scale precipitation fields  $P(X, Y, t)$  is considered reliable at spatial scales larger than a fixed reliability scale  $L_0$ . The reliability scale can be greater than or equal to the nominal spatial resolution of the large-scale fields; precipitation fields are either unknown or unreliable at smaller scales. The RainFARM approach aims at generating synthetic downscaled fields at these smaller spatial scales. This is achieved by extrapolating to small scales the spatial power spectrum of the large-scale field,  $|\hat{P}(K_x, K_y, t)|^2$ , where  $(K_x, K_y)$  are the spatial wavenumbers and  $\hat{P}$  is the spatial Fourier transform of  $P$ . The spatial power spectrum at small scales is assumed to have a power-law dependence on wavenumber, with spectral slope  $\alpha$ . The value of  $\alpha$  can be derived by extrapolation of the slope obtained from a fit to the spectrum of the large-scale field or fixed by resorting to a library of observed spectral slopes of precipitation data. For simplicity, we assume spatial isotropy in the two spatial directions; this assumption can be easily relaxed if needed. In the following, we will use capitalized coordinates and wavenumbers  $(X, Y, K_x, \text{ and } K_y)$  to refer to large-scale quantities (larger than or equal to  $L_0$ ) and lowercase letters  $(x, y, k_x, \text{ and } k_y)$  when considering all scales. The spatial downscaling procedure is then applied separately to each time step.

In detail, the steps of the modified procedure at each time  $t$  are as follows:

- (i) Generate Gaussianized fields,  $P_g(X, Y, t) = f[P(X, Y, t)]$ , characterized by a Gaussian amplitude distribution. Rank ordering is a simple Gaussianization method that can be used for this purpose (Schreiber and Schmitz 1996).
- (ii) Estimate the spatial Fourier spectrum of the Gaussianized field  $\hat{P}_g(K_x, K_y, t)$ .
- (iii) Generate a synthetic spatial Fourier spectrum at all scales  $\hat{g}(k_x, k_y, t)$ . This is a power-law spectrum with fixed logarithmic slope  $\alpha$  and amplitude  $|\hat{g}(k_x, k_y, t)|^2 \propto (k_x^2 + k_y^2)^{-\alpha/2}$ . Random, uniformly distributed phases are assigned to this spectrum.
- (iv) Merge spectra and generate a new Fourier spectrum that has the Fourier spectrum of the original field  $P$  at large scales and the synthetic spectrum at small scales,

$$\hat{s}(k_x, k_y, t) = \begin{cases} \hat{P}_g(K_x, K_y, t), & \text{if } k \leq k_0 \\ \frac{|\hat{P}_g(k_0)|}{|\hat{g}(k_0)|} \hat{g}(k_x, k_y, t), & \text{if } k > k_0 \end{cases},$$

where the small-scale synthetic spectrum has been normalized to match the large-scale spectrum at wavenumber  $k_0 = 2\pi L_{\max}/L_0$  and  $\hat{P}_g(k_0)$  and  $\hat{g}(k_0)$  are radially averaged spectra. Here,  $k = \sqrt{k_x^2 + k_y^2}$  is the radial wavenumber.

- (v) Apply the inverse Fourier transform to  $\hat{s}(k_x, k_y, t)$  and generate the field  $s(x, y, t)$ . Because we conserved Fourier amplitudes and phases at large scales, at large scales the spatial structure of  $s$  is equal to that of  $P_g$ .

The following two steps do not differ from the standard RainFARM procedure:

- (vi) A final nonlinear transformation: A simple exponential has proven to work well,

$$\tilde{r}(x, y) = \exp[\gamma s(x, y)].$$

In principle, the parameter  $\gamma$  is free, but a value  $\gamma = 1$  has been successfully used in past applications and it has been adopted in this work.

- (vii) Even though the large-scale structure of the field  $s$  is equal to that of  $P_g$ , application of the nonlinear transformation mixes Fourier components and slightly scrambles the large-scale Fourier phases. For this reason, the large-scale structure of the reconstructed field  $\tilde{r}$  is not exactly equal to  $P$ . We thus continue to apply a consistency condition between the synthetic field  $\tilde{r}$  and the original field  $P$ , as in the original RainFARM method. If we

indicate with  $\tilde{R}(X, Y) = \langle \tilde{r}(x, y) \rangle_{L_0}$  the coarse graining (aggregation, indicated with angle brackets) of the  $\tilde{r}$  field at scale  $L_0$ , we can define a new field

$$r(x, y) = \tilde{r}(x, y)P(X, Y)/\tilde{R}(X, Y).$$

The  $r(x, y)$  field, which represents the output of the downscaling procedure, has the property that, when aggregated at the scale  $L_0$ , it is identical to the original field,  $\langle r(x, y) \rangle_{L_0} = P(X, Y)$ .

By construction, this downscaling procedure is able to conserve the large-scale features of the original precipitation field down to the reliability scales. At the same time, the model is able to correctly reproduce the small-scale statistics of precipitation (e.g., the spatiotemporal correlation structure of the main statistical moments and the scaling properties of precipitation). Stochastic variability is generated only at scales smaller than the reliability scale  $L_0$ .

The advantage of the modified RainFARM procedure is to have, prior to steps (vi) and (vii), a spatial distribution of the downscaled stochastic field that is rather similar to that of the original field. In the standard procedure, a completely synthetic power-law spectrum was generated at all scales and the resultant high-resolution field was forced only at the end of the procedure to be consistent with the original large-scale field. When used for purely spatial downscaling, this choice introduces sharp gradients and raster-like features in the resulting precipitation field and an artificial oscillation in the spatial Fourier spectrum at scales just below the reliability scale. The power spectrum obtained by the application of the modified RainFARM procedure does not show such spurious features and is more similar to the spatial power spectrum of observed precipitation fields.

The RainFARM procedure was developed to produce ensemble forecasts: for each choice of the set of random phases in the Fourier spectrum, a different field is generated. By considering a large number of possible choices of the set of Fourier phases, a whole ensemble of small-scale precipitation fields can be created, which allow for assessing probabilities of occurrence of extreme rainfall and/or of the associated hydrological response. Here, because we compare probability density functions (PDFs) obtained from a large number of rain gauges and from a large number of different times, to keep the same statistics we perform only one downscaling for each time step.

## 4. Precipitation climatology

### a. Results from Protheus

We first compare the precipitation output from the Protheus system to the observed precipitation, upscaled

(coarse grained) at the model resolution. To this end, for each model pixel containing at least one station, we compute the average of all observations in that pixel. Figure 2a shows the observed (dashed line) and modeled (solid line) annually averaged time series of total precipitation over the study area from 1958 to 2001. The time series have been obtained by area averaging the model data and the upscaled station data only over pixels containing observations. While there is a good correlation in the interannual fluctuations, Protheus tends to overestimate average precipitation with respect to the observations. This overestimation occurs in almost all pixels considered, as shown by Fig. 2b, which reports a scatterplot of the modeled and observed total precipitation, averaged over the whole time period (1958–2001), for each pixel (one point for each model pixel).

Interannual fluctuations are coherently reproduced by the model; the correlation coefficient between the two time series is 0.79, which is statistically significant at the 95% confidence level. Statistical significance against the null hypothesis of no correlation has been determined (here and elsewhere in the paper) using a Monte Carlo method based on randomly shuffling the modeled series in time (1000 realizations were used). The interannual variability modeled by the RCM appears to follow that of its large-scale forcing field, ERA-40 (discussed below). For each individual pixel, the time series of yearly averaged modeled precipitation show a statistically significant correlation with observed precipitation time series. As shown in Fig. 2c, correlations as high as 0.65 are maintained as long as a pixel contains at least five rain gauges, while for pixels with fewer rain gauges the correlations decrease and the spread increases.

There is a significant seasonal dependence in these correlations. Figure 2d shows the annual cycle of the correlation coefficients between the modeled and observed monthly mean precipitation, for individual pixels (gray lines) and for the whole domain average (black line). The highest correlation occurs during spring and autumn, the periods during which weather perturbations over the study area are mainly of synoptic origin. Correlations are significantly lower during summer, when the Piedmont and Valle d'Aosta regions are subject to localized thunderstorms. This type of event cannot be modeled by a limited-resolution hydrostatic model such as Protheus, and its correct parameterization is a difficult task for all current RCMs. The temporal power spectra of the Protheus precipitation (not shown) are characterized by a significant peak at one day during summer, confirming that during this season there is a strong daily cycle of precipitation presumably associated with thunderstorm activity. The diurnal periodicity disappears in winter, owing to the prevalence of large-scale precipitation of



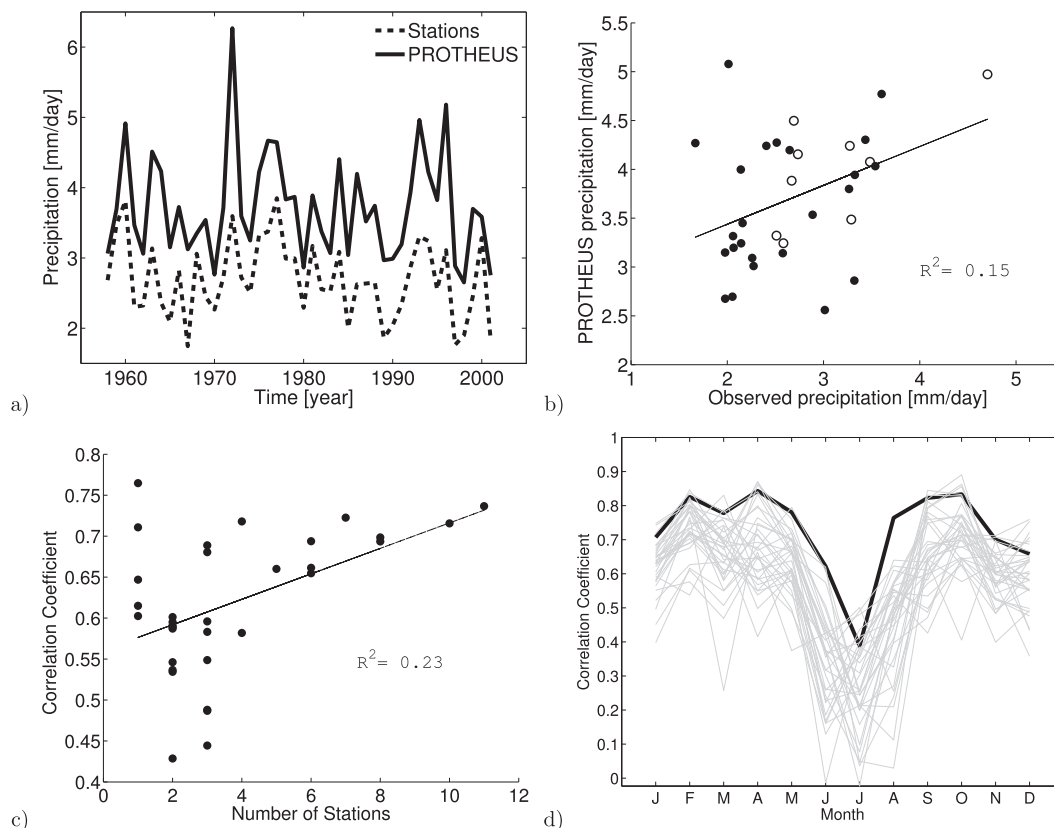


FIG. 2. (a) Area-averaged time series of annual precipitation from Protheus (solid line) and rain gauge observations aggregated at the Protheus resolution (dashed line). (b) Scatterplot of Protheus vs observed precipitation, averaged over the period 1958–2001 (one point for each model pixel). Empty symbols denote pixels with more than four rain gauges. (c) Correlation coefficients between modeled and observed annual precipitation averages for each model pixel, as a function of the number of rain gauges included in the pixel. (d) Annual cycle of the correlation coefficient between Protheus precipitation and observed rainfall for each model pixel (gray lines) and for the area average over all pixels (black line). Also shown in (b), (c) is the linear fit between the two datasets and the coefficient of determination  $R^2$ .

synoptic-scale origin. As further discussed below, a signature of these different precipitation regimes is seen also in the downscaled model output and in particular in the slopes of the spatial power spectra.

Table 1 (first two rows) summarizes the comparison of total precipitation, precipitation intensity, number of dry days (defined as days with precipitation  $< 1 \text{ mm day}^{-1}$ ), precipitation variance, and the 99th percentile of precipitation, for Protheus and for the upscaled observations over the study area. While Protheus slightly overestimates the total precipitation, as well as its variance and the 99th percentile of precipitation compared to observations, precipitation intensity and the percentage of dry days are slightly lower in the model than in observations. This suggests that rain events are slightly weaker and more frequent in Protheus than in reality.

Overestimation of Protheus precipitation in the Alpine region has already been reported in Artale et al. (2010). In particular, compared to precipitation data from

ERA-40 and the Climate Research Unit (CRU) data, Protheus was found to produce too much orographic precipitation, possibly because of a systematic overestimation during winter over the northern flank of Alps, associated with the passage of cyclones over central Europe and a possible enhanced intensification of cyclones in the Protheus domain in winter.

#### b. Results from ERA-40

A similar analysis can be performed for ERA-40 precipitation. Also in this case, observed precipitation was averaged over all stations contained in each ERA-40 grid element (pixel). Some of the ERA-40 pixels overlap only partially with the region where the rain gauges are located and with the Protheus pixels considered above. For this reason, the areal mean of the ERA-40 signal has been computed by weighting each pixel by the fraction of area that overlaps with the analyzed Protheus pixels (i.e., which contain rain gauges).

TABLE 1. Averages (over space and time), over pixels containing rain gauges, of total precipitation, daily precipitation intensity (daily precipitation averaged only over rainy days), percentage of dry days, variance, and 99th percentile of precipitation. Dry days are defined as days with precipitation  $<1 \text{ mm day}^{-1}$ ; rainy days have precipitation greater than  $1 \text{ mm day}^{-1}$ . From top to bottom: statistics for the Protheus model outputs, for the observations upscaled to the Protheus resolution, for ERA-40, for the observations upscaled to the ERA-40 resolution, for the downscaled Protheus and ERA-40 fields, and for individual rain gauge stations.

	$\langle \bar{P} \rangle \text{ (mm day}^{-1}\text{)}$	$\langle \bar{P} \rangle_{\text{wet}} \text{ (mm day}^{-1}\text{)}$	Dry days	$\sigma^2 \text{ (mm day}^{-1}\text{)}^2$	99th percentile $\text{(mm day}^{-1}\text{)}$
Protheus	3.7	9.3	61%	73.65	41.26
Obs_Protheus	2.7	10.0	73%	66.30	38.67
ERA-40	2.1	5.8	66%	18.20	19.94
Obs_ERA-40	2.7	8.4	68%	52.58	35.65
Downscaled Protheus	3.9	10.2	62%	105.71	48.4
Downscaled ERA-40	2.2	6.4	67%	29.16	24.9
Stations	2.9	12.4	77%	96.85	46.0

Figure 3a shows the annually and spatially averaged time series of total precipitation from 1958 to 2001 for ERA-40 and for the observations. ERA-40 precipitation is lower than the coarse-grained observed precipitation at the ERA-40 resolution. Interannual variability is well

represented in the reanalyses (except in the years between 1965 and 1970) but the average correlation coefficient (0.5; statistically significant at 95% confidence level) is lower than for Protheus (0.8). The lower correlation between ERA-40 and the observations could be

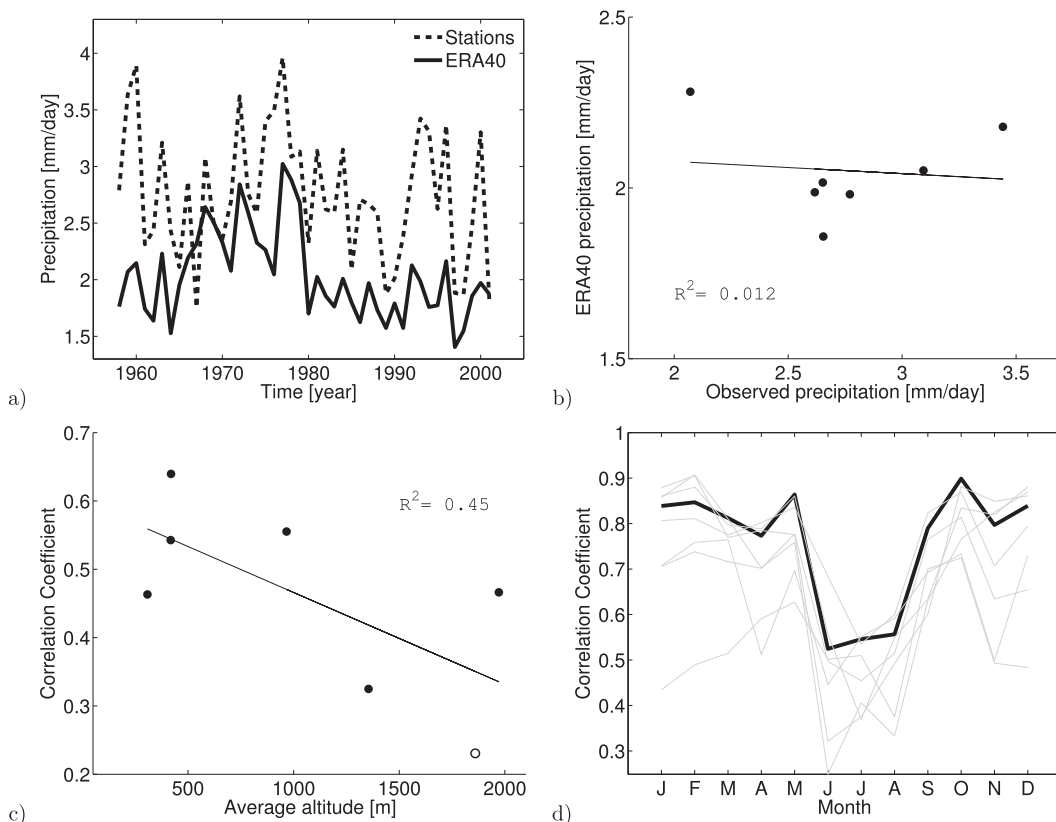


FIG. 3. (a) Area-averaged time series of annual precipitation from ERA-40 (solid line) and the rain gauge observations aggregated at the ERA-40 resolution (dashed line). (b) Scatterplot of ERA-40 vs observed rainfall, averaged over the period 1958–2001 (one point for each ERA-40 pixel). (c) Correlation coefficients between ERA-40 and observed annual precipitation averages, for each ERA-40 pixel, as a function of the average altitude in each pixel (provided by a digital elevation model). The correlation coefficient shown with the empty symbol is not statistically significant at the 95% confidence level. (d) Annual cycle of the correlation coefficient between ERA-40 precipitation and observed rainfall for each ERA-40 pixel (gray lines) and for the area average over all pixels (black line). Also shown in (b),(c) is the linear fit between the two datasets and the  $R^2$ .



attributed to the coarser resolution of the reanalysis product with respect to that of the RCM, a relevant issue in such an orographically complex area. In fact, the correlation between the time series of yearly averaged precipitation from ERA-40 and the upscaled observations calculated for each ERA-40 pixel (shown in Fig. 3c as a function of the pixel altitude) indicates that the higher the average pixel altitude, the lower the correlation coefficient value. Figure 3d shows the annual cycle of the correlation coefficient between ERA-40 and the observed precipitation for each pixel (gray lines) and for the entire domain (black line). As already noted for Protheus, also in this case there is a summer minimum in correlation (May–July), possibly associated with difficulties in the reanalysis to reproduce strong convective events in summer. In other months, the correlation can be as high as 0.8.

The third and fourth rows in Table 1 compare the average total precipitation, precipitation intensity, number of dry days, precipitation variance, and 99th percentile of precipitation in ERA-40 and in the upscaled observations. Compared to the observed precipitation statistics, ERA-40 strongly underestimates the precipitation intensity, the variance, and the 99th percentile of data, while total precipitation is slightly lower than the observed one and the percentage of dry days is approximately the same.

### c. Distribution of daily precipitation

Figures 4a–d show the PDFs of total daily precipitation for the Protheus model and for the upscaled observations, for the individual seasons: December–February (DJF), March–May (MAM), June–August (JJA), and September–November (SON). Figure 4e shows the annually averaged daily precipitation PDFs. Jackknife subsampling has been used to determine the 5% and 95% for each PDF, by estimating the distributions from random subsamples of the data containing half of the available data. Overall, we find a good agreement between the PDFs produced by the model and the upscaled observations, both on an annual and a seasonal basis, and the ranges induced between the 5th and 95th percentiles of the distributions largely overlap.

The main disagreement between the modeled and observed PDFs occurs in winter (Fig. 4a) when Protheus shows a wider distribution, with a larger number of intense events. As discussed above, this discrepancy can be associated with the behavior of wintertime atmospheric circulation and cyclone intensification in this specific RCM.

Figures 4a–e also report the average PDFs obtained from individual rain gauges. Except in winter, the PDFs of total precipitation from Protheus display significantly

lower tails compared to the PDFs from the individual rain gauges, as expected by the coarser resolution and averaging process intrinsic in the model. In fact, the model cannot capture precipitation extremes, which are often quite localized in space. The total precipitation from the model rarely reaches values larger than  $100 \text{ mm day}^{-1}$ , while observed values can be as high as  $250\text{--}300 \text{ mm day}^{-1}$  (even  $350 \text{ mm day}^{-1}$  in winter). This is also confirmed by Fig. 4f, which compares the probabilities of exceedance for the observations, the upscaled observations, and the Protheus output, obtained by sorting the precipitation data and plotting the rank in the sorted series versus the corresponding amplitudes. While there is good agreement between the upscaled observations and the Protheus data up to amplitudes of about  $100 \text{ mm day}^{-1}$ , rare events, with higher amplitudes, are underestimated by the Protheus model.

To correctly represent small-scale intense precipitation, a further downscaling step is required, which is achieved by resorting to the RainFARM procedure.

## 5. Stochastic downscaling

### a. Downscaling Protheus RCM precipitation

An important aspect of the RainFARM procedure is the choice of the spectral slopes. Because precipitation patterns over the focus region are different in different seasons, we compute the seasonally averaged logarithmic slopes  $\alpha$  and use them to extrapolate the power spectrum from the resolved to the unresolved small scales, assuming isotropy in the two spatial directions. We find an approximate power-law behavior of the spectrum in the range of scales  $69 < \lambda < 160 \text{ km}$ , from which the different logarithmic slopes, reported in Table 2, have been estimated. The different values of  $\alpha$  during summer and winter are indicative of the different precipitation regimes in different seasons.

The Protheus data have been downscaled in space down to  $0.9 \text{ km}$ , which previous studies have shown to be adequate for a direct comparison with observations (Brussolo et al. 2008), following the procedure illustrated in section 3 and assuming the model nominal resolution as the reliability scale. For each rain gauge, the time series from the closest downscaled pixel was then used for the comparison with the observed precipitation statistics.

Figures 5a–d show the seasonally averaged PDFs of total precipitation from the downscaled model output (black) and individual rain gauge observations (red), and Fig. 5e shows the annually averaged PDFs. The agreement between the downscaled model PDFs and the observations is excellent in spring, summer, and autumn, the most significant seasons in terms of precipitation in

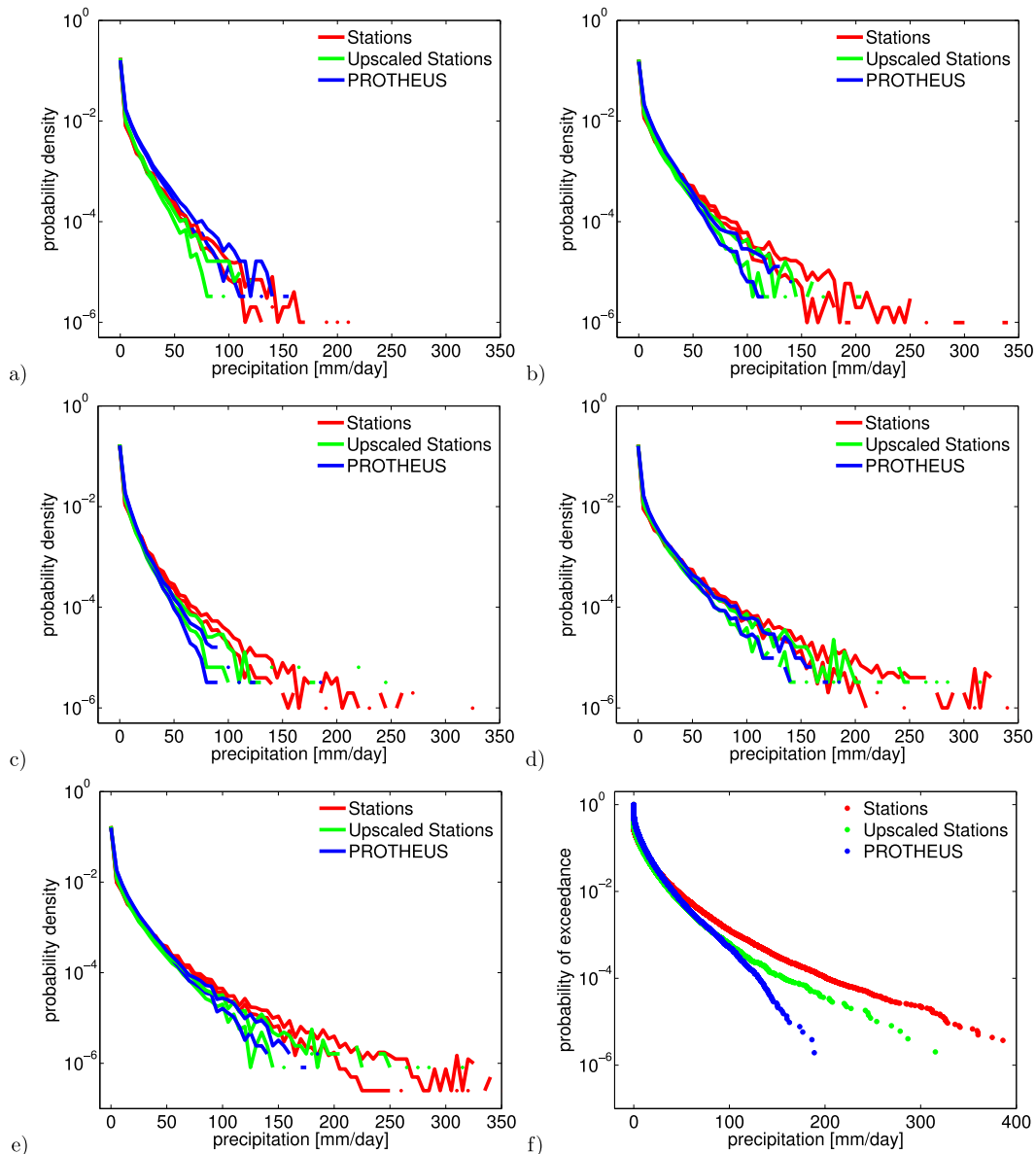


FIG. 4. Daily precipitation PDFs of Protheus rainfall (blue lines), rain gauge observations upscaled to Protheus resolution (green lines), and data from individual rain gauges (red lines). The PDFs for individual seasons: (a) DJF, (b) MAM, (c) JJA, and (d) SON. (e) The annually averaged daily precipitation PDFs. The two lines for each PDF indicate the 5th and 95th percentiles in each class. (f) The probability of exceedance of total daily precipitation for Protheus (blue lines), for rain gauge observations upscaled to Protheus resolution (green lines), and for data from individual rain gauges (red lines). Beyond the value of  $400 \text{ mm day}^{-1}$ , individual rain gauges recorded five precipitation events up to  $700 \text{ mm day}^{-1}$  (not shown).

the area under study. This shows that the RainFARM downscaling procedure is capable of generating precipitation amplitude distributions comparable with the PDFs of real observations, starting from the RCM output for the region of interest. Similarly to what we observed in Fig. 4a, also in this case precipitation is overestimated in winter, with the downscaled fields showing more frequent extreme events compared to the observations. In this case,

the overestimation of Protheus in winter has been propagated by the downscaling procedure, resulting in overestimated extremes.

To show how much of the observed precipitation variance is present in the Protheus downscaled precipitation fields, we show in Fig. 6a the scatterplot of the downscaled model and observed precipitation variance for each small-scale pixel. RainFARM works quite

TABLE 2. Logarithmic slope  $\alpha$  of the spatial power spectrum of the Protheus and ERA-40 precipitation fields for each season (climatological mean).

	Protheus	ERA-40
DJF	2.15	1.82
MAM	1.64	1.80
JJA	0.92	1.38
SON	1.74	1.79

efficiently in preserving the observed precipitation variance when it is applied to the Protheus precipitation fields (the linear regression between the two series indicates an  $R^2 = 0.44$ ), as it is also clear looking at the values reported in Table 1.

We further explore the ability of the downscaling procedure in reproducing precipitation extremes looking at the exceedance probability of given precipitation levels (Fig. 5f) and comparing the 99th percentile of the observations with that of the downscaled model fields (Fig. 6b). Figure 5f shows that there is an excellent agreement between the two curves, confirming that precipitation extremes in the downscaled model output have the same probability of occurrence as in the observations from individual rain gauges. The 99th percentile of the observed and downscaled precipitation data are positively correlated, with the linear fit between the two datasets being characterized by  $R^2 = 0.51$ .

Table 1 (fifth and seventh rows) summarizes the averages, over space and time, of the analyzed precipitation statistics for the downscaled Protheus output and for the individual rain gauge observations. While there is not a significant difference in the values of total precipitation, precipitation intensity and number of dry days before and after application of the downscaling procedure, indicating that this downscaling method is not able to correct large-scale biases in the precipitation fields, it is quite clear from Table 1 that the downscaling acts more effectively on the precipitation variance and precipitation extremes. By using a different threshold to define dry days in the Protheus field ( $3.5 \text{ mm day}^{-1}$ ) one obtains a percentage of dry days in the model which is comparable to the observed one.

### b. Downscaling ERA-40 precipitation

It is interesting to verify the performance of the RainFARM downscaling procedure when directly applied to the large-scale precipitation fields, without the intermediation of the dynamical downscaling by a RCM.

Figure 7a shows the precipitation PDFs from ERA-40 and from the rain gauge observations upscaled to the ERA-40 resolution for the whole year. Especially above  $\sim 15 \text{ mm day}^{-1}$ , ERA-40 underestimates the frequency

of intense rainfall events when compared to the upscaled observations.

By downscaling ERA-40 precipitation, assuming that the reliability scale is equal to the nominal spatial resolution of the reanalysis, we obtain new fields having a spatial resolution of about 1 km. Table 2 shows the seasonal logarithmic slopes  $\alpha$  of the spatial power spectra used in the downscaling procedure; the logarithmic spectral slopes are estimated from an extremely limited range of scales, in the interval  $264 < \lambda < 528 \text{ km}$ . Figure 7b shows that the distribution of downscaled ERA-40 fields is wider than the original one, but still underestimates the probability of occurrence of intense precipitation events, at all amplitudes. The results are similar if the analysis is repeated at seasonal scale (not shown). Figures 7c and 7d confirm that the variance and the 99th percentile of the downscaled ERA-40 precipitation in each downscaled pixel are underestimated compared with those of the individual observations. As for the Protheus case, the average precipitation, the precipitation intensity and the percentage of dry days do not change substantially after application of the downscaling procedure (Table 1), owing to the fact that RainFARM is not designed to correct large-scale biases.

Variations in the values of the logarithmic spectral slopes (e.g., by considering the  $\alpha$  values estimated from the Protheus fields rather than from ERA-40 fields) do not produce different ERA-40 downscaled precipitation outputs.

## 6. Discussion and conclusions

In this work, we have analyzed the precipitation output of a state-of-the-art regional climate model, the Protheus system, and of its large-scale driver, ERA-40. Both Protheus and ERA-40 have been spatially downscaled using a modified version of the RainFARM procedure, originally devised for spatiotemporal downscaling of the output of limited-area atmospheric models. The downscaled precipitation fields produced by the modified RainFARM method have spatial power spectra more similar to observed precipitation spectra and are less prone to possible artifacts than the fields generated by the original RainFARM procedure when used for purely spatial downscaling. This RainFARM variant looks suitable for spatial downscaling of the output of climate models and hence for climate change impact studies.

The RainFARM stochastic downscaling procedure, when applied to the rainfall fields produced by the Protheus RCM with spatial resolution of 30 km, generates rainfall fields with small-scale statistics (precipitation variance, 99th percentile of precipitation values and PDFs), which are very similar to those of the observations and

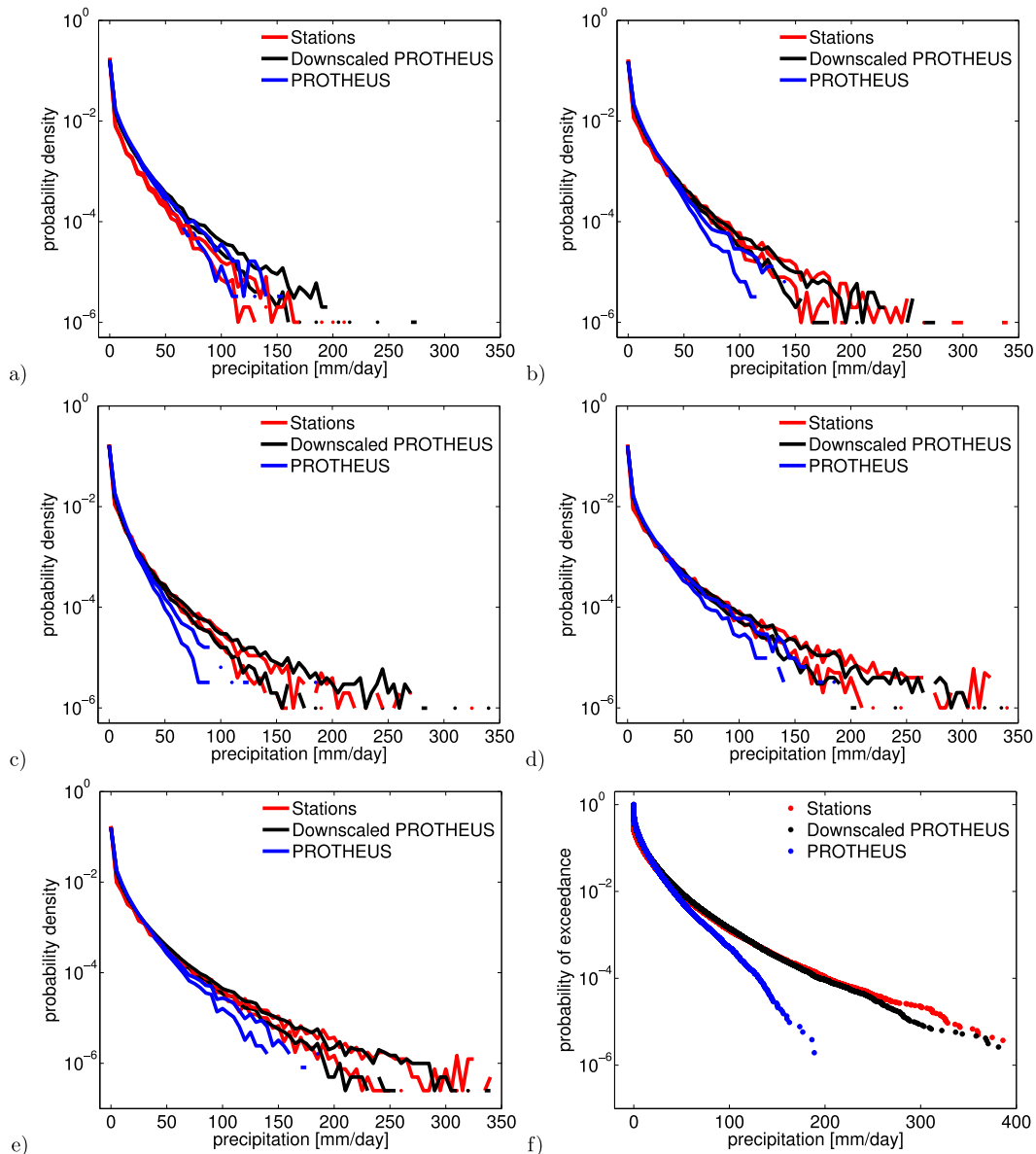


FIG. 5. Daily precipitation PDFs of ProtHeus rainfall (blue lines), data from individual rain gauges (red lines), and downscaled ProtHeus fields (black lines). The PDFs for individual seasons: (a) DJF, (b) MAM, (c) JJA, and (d) SON. (e) The annually averaged daily precipitation PDFs. The two lines for each PDF indicate the 5th and 95th percentiles in each class. (f) The probability of exceedance of total daily precipitation for ProtHeus (blue lines), for data from the individual rain gauges (red lines), and for the downscaled ProtHeus fields (black lines). Beyond the value of  $400 \text{ mm day}^{-1}$ , individual rain gauge data have five precipitation events up to  $700 \text{ mm day}^{-1}$  and the downscaled ProtHeus precipitation field has one event beyond  $700 \text{ mm day}^{-1}$  (not shown).

are characterized by the right probability of intense rainfall events during most of the year. On the other hand, biases introduced by the RCM at large scales, such as an overall overestimation of the total precipitation, underestimation of the number of dry days, and the disagreement in the frequency of precipitation events, particularly during the winter season, are not corrected by the stochastic downscaling procedure. When RainFARM

is directly applied to the larger-scale ERA-40 fields, with a spatial resolution of about 120 km in the study area, one obtains a significant improvement in the statistics of intense rainfall but the tails in the distribution are not fully reproduced. This result indicates that downscaling procedures such as RainFARM perform in a better way when they are applied to rainfall fields with mesoscale resolution. At larger scales, the effects of

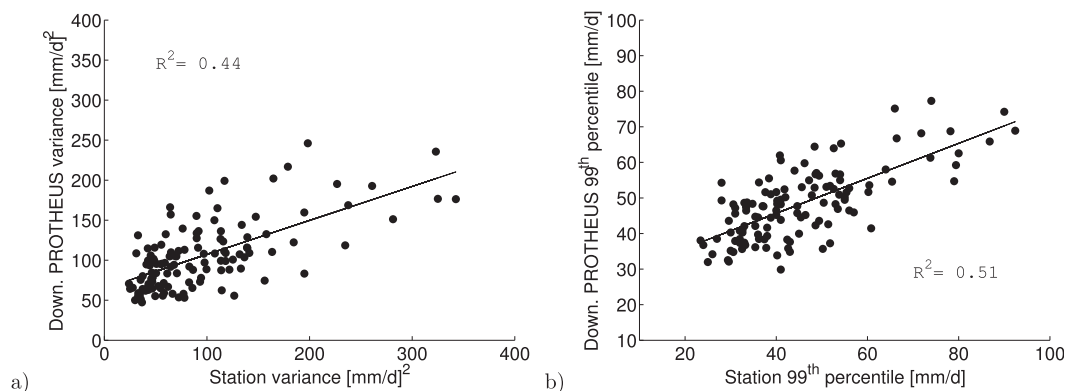


FIG. 6. Scatterplots of (a) precipitation variance of downscaled Protheus vs individual stations (one point for each downscaled model pixel corresponding to each rain gauge location) and (b) 99th percentile of downscaled Protheus precipitation vs individual stations. Both plots show the linear fit between the two series along with the  $R^2$  value.

orography inside the model box might matter, calling for rainfall downscaling with subgrid topographic effects included. Currently, the RainFARM procedure employed in this study does not account for these

effects. These results also confirm the added value of nesting a RCM into a larger-scale GCM or a global reanalysis or, alternatively, of running CGMs at higher resolution.

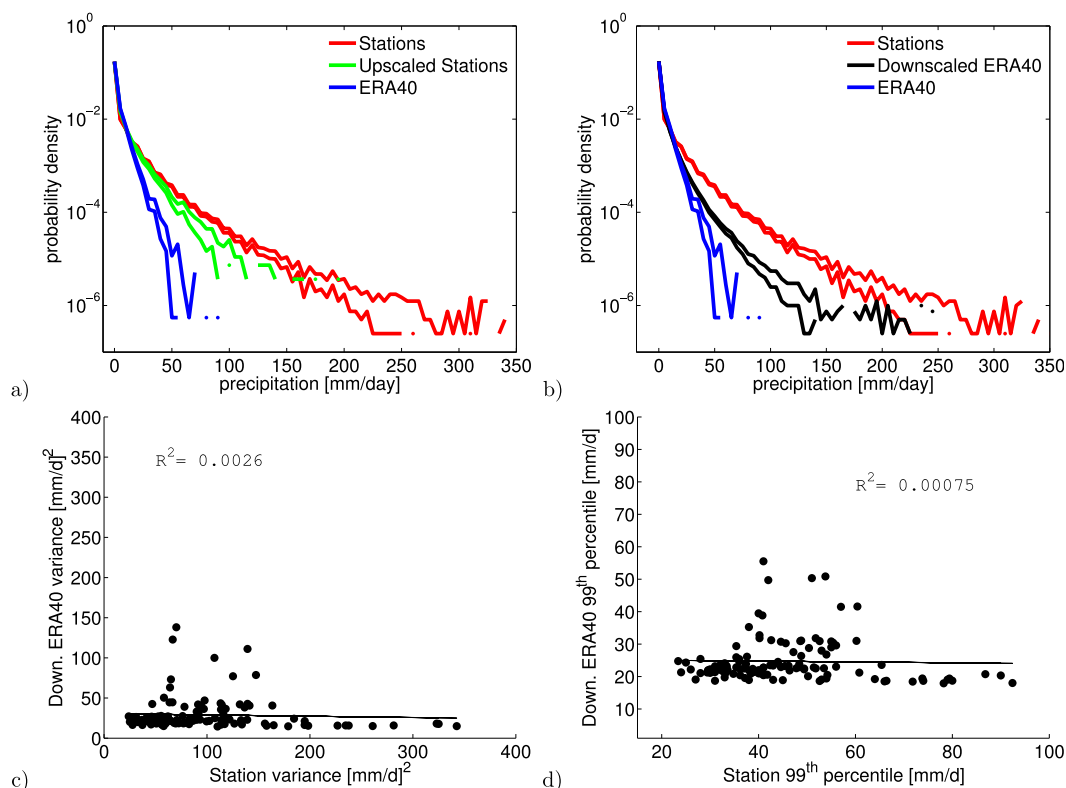


FIG. 7. (a) Daily precipitation PDFs of ERA-40 rainfall (blue lines), rain gauge observations upscaled at ERA-40 resolution (green lines), and data from individual rain gauges (red lines). (b) Daily precipitation PDFs of ERA-40 rainfall (blue lines), data from individual rain gauges (red lines), and downscaled ERA-40 fields (black lines). The individual PDFs of ERA-40 daily precipitation in each pixel were weighted by the number of Protheus pixels falling within the ERA-40 pixel. (c) Scatterplot of precipitation variance of downscaled ERA-40 vs individual stations (one point for each downscaled model pixel corresponding to each rain gauge location). (d) Scatterplot of 99th percentile of downscaled ERA-40 precipitation vs individual stations. The scatterplots show the linear fit between the two series along with the  $R^2$  value.

We also explored the sensitivity of the results to parameter changes. The downscaling procedure has very few free parameters. In particular, the results of the downscaling procedure for Protheus and ERA-40 have been obtained using  $\gamma = 1$  in the nonlinear transformation [see (vi) in section 5]. We tested the sensitivity of the method to changes in  $\gamma$  (considering  $\gamma = 0.8, 0.5$ , and  $0.25$ ) and did not observe noticeable changes in the PDFs of the downscaled precipitation. Similar results were obtained by changing the value of  $\alpha$ , the spatial logarithmic slope of the spatial power spectrum. For example, we used  $\alpha = 2.0$  ( $\alpha = 1.70$  and  $2.5$ ) to downscale the Protheus autumn (winter) precipitation fields, obtaining small-scale precipitation PDFs very similar to those obtained using the logarithmic slope directly calculated from the large-scale precipitation spectrum. The dependence of the downscaled precipitation on the value of  $\alpha$  in the ERA-40 case has been assessed using the Protheus-based  $\alpha$  values to downscale the reanalysis fields. Again, the downscaled ERA-40 fields do not show noticeable changes, and their statistics still do not compare well with the precipitation statistics from rain gauge observations. These results indicate that the properties of the downscaled precipitation field are mostly influenced by the characteristics of the large-scale field, especially in view of the fact that RainFARM imposes consistency between the large-scale field and the large-scale behavior of the downscaled precipitation.

An important point concerns the quality of the model fields to be stochastically downscaled. In its current version, RainFARM has not been designed to correct large-scale biases in the model precipitation fields. A good agreement of upscaled observations with model data, in terms of amplitude distributions, is an important prerequisite for the successful application of the downscaling procedure. In the case of the Protheus RCM, the spring, summer, and autumn model precipitation fields are characterized by amplitude distributions that compare well with the observations, when upscaled to the same resolution. In these seasons, the downscaling procedure is capable of reconstructing the missing variance and creating small-scale precipitation fields, which are directly comparable to observations at the rain gauge scale, whereas the Protheus overestimation of winter precipitation is propagated, by the downscaling procedure, also at small scales. The agreement between the statistics of the global ERA-40 fields and that of the upscaled observations is lower, and the downscaling produces small-scale rainfall statistics that, while closer to what was found from rain gauge data, have smaller variance. This is probably part of the reason why we find a better agreement with the rain gauge observations by downscaling Protheus rather than its driver, ERA-40.

As a conclusion, the results reported here indicate that stochastic rainfall downscaling is an efficient method for generating small-scale precipitation fields with the correct statistical properties from long-term climate simulations. This approach does not require extrapolation of current conditions to future situations, as the small-scale statistical properties of rainfall are determined only by the behavior of the model-generated fields at larger scales. Stochastic rainfall downscaling can thus be easily applied to climate scenarios for impact studies, provided the models produce precipitation fields with correct large-scale behavior.

**Acknowledgments.** This work has been funded by the Project of strategic Interest *NextData* of the Italian Ministry of Education, University and Research (MIUR) (<http://www.nextdataproyect.it>) and by the PRIN 2010–11 projects “Innovative methods for water resources management and risk assessment under uncertainty” and 20108 TZKHC.

## REFERENCES

- Artale, V., and Coauthors, 2010: An atmosphere–ocean regional climate model for the Mediterranean area: Assessment of a present climate simulation. *Climate Dyn.*, **35**, 721–740, doi:10.1007/s00382-009-0691-8.
- Brussolo, E., J. von Hardenberg, L. Ferraris, N. Rebora, and A. Provenzale, 2008: Verification of quantitative precipitation forecasts via stochastic downscaling. *J. Hydrometeorol.*, **9**, 1084–1094, doi:10.1175/2008JHM994.1.
- , —, and N. Rebora, 2009: Stochastic versus dynamical downscaling of ensemble precipitation forecasts. *J. Hydrometeorol.*, **10**, 1051–1061, doi:10.1175/2009JHM1109.1.
- Castro, C. L., R. A. Pielke Sr., and G. Leoncini, 2005: Dynamical downscaling: Assessment of value retained and added using the Regional Atmospheric Modeling System (RAMS). *J. Geophys. Res.*, **110**, D05108, doi:10.1029/2004JD004721.
- Chiew, F., D. Kirono, D. Kent, A. Frost, S. Charles, B. Timbal, K. Nguyen, and G. Fu, 2010: Comparison of runoff modelled using rainfall from different downscaling methods for historical and future climates. *J. Hydrol.*, **387**, 10–23, doi:10.1016/j.jhydrol.2010.03.025.
- Ciccarelli, N., J. von Hardenberg, A. Provenzale, C. Ronchi, A. Vargiu, and R. Pelosini, 2008: Climate variability in north-western Italy during the second half of the 20th century. *Global Planet. Change*, **63**, 185–195, doi:10.1016/j.gloplacha.2008.03.006.
- Dell'Aquila, A., S. Calmanti, P. M. Ruti, M. V. Struglia, G. Pisacane, A. Carillo, and G. Sannino, 2012: Effects of seasonal cycle fluctuations in an A1B scenario over the Euro-Mediterranean region. *Climate Res.*, **52**, 135–157, doi:10.3354/cr01037.
- Dubois, C., and Coauthors, 2012: Future projections of the surface heat and water budgets of the Mediterranean Sea in an ensemble of coupled atmosphere–ocean regional climate models. *Climate Dyn.*, **39**, 1859–1884, doi:10.1007/s00382-011-1261-4.
- Ferraris, L., S. Gabellani, U. Parodi, N. Rebora, J. von Hardenberg, and A. Provenzale, 2003a: Revisiting multifractality in rainfall fields. *J. Hydrometeorol.*, **4**, 544–551, doi:10.1175/1525-7541(2003)004<0544:RMIRF>2.0.CO;2.



- , —, N. Rebora, and A. Provenzale, 2003b: A comparison of stochastic models for spatial rainfall downscaling. *Water Resour. Res.*, **39**, 1368, doi:10.1029/2003WR002504.
- Flaounas, E., P. Drobinski, M. Vrac, S. Bastin, C. Lebeaupin-Brossier, M. Stéfanon, M. Borga, and J. Calvet, 2012: Precipitation and temperature space–time variability and extremes in the Mediterranean region: Evaluation of dynamical and statistical downscaling methods. *Climate Dyn.*, **40**, 2687–2705, doi:10.1007/s00382-012-1558-y.
- Gabellani, S., G. Boni, L. Ferraris, J. von Hardenberg, and A. Provenzale, 2007: Propagation of uncertainty from rainfall to runoff: A case study with a stochastic rainfall generator. *Adv. Water Resour.*, **30**, 2061–2071, doi:10.1016/j.advwatres.2006.11.015.
- Giorgi, F., 1990: Simulation of regional climate using a limited area model nested in a general circulation model. *J. Climate*, **3**, 941–964, doi:10.1175/1520-0442(1990)003<0941:SORCUA>2.0.CO;2.
- , 2006: Regional climate modeling: Status and perspectives. *J. Phys. IV France*, **139**, 101–118, doi:10.1051/jp4:2006139008.
- , G. Bates, and S. Nieman, 1993a: The multiyear surface climatology of a regional atmospheric model over the western United States. *J. Climate*, **6**, 75–95, doi:10.1175/1520-0442(1993)006<0075:TMSCOA>2.0.CO;2.
- , M. Marinucci, and G. Bates, 1993b: Development of a second generation regional climate model (RegCM2). Part I: Boundary layer and radiative transfer processes. *Mon. Wea. Rev.*, **121**, 2794–2813, doi:10.1175/1520-0493(1993)121<2794:DOASGR>2.0.CO;2.
- Gualdi, S., and Coauthors, 2013: The CIRCE simulations: Regional climate change projections with realistic representation of the Mediterranean Sea. *Bull. Amer. Meteor. Soc.*, **94**, 65–81, doi:10.1175/BAMS-D-11-00136.1.
- Guyennon, N., E. Romano, I. Portoghesi, F. Salerno, S. Calmanti, A. B. Petrangeli, G. Tartari, and D. Copetti, 2013: Benefits from using combined dynamical–statistical downscaling approaches—Lessons from a case study in the Mediterranean region. *Hydrol. Earth Syst. Sci.*, **17**, 705–720, doi:10.5194/hess-17-705-2013.
- Maraun, D., and Coauthors, 2010: Precipitation downscaling under climate change: Recent developments to bridge the gap between dynamical models and the end user. *Rev. Geophys.*, **48**, RG3003, doi:10.1029/2009RG000314.
- Marshall, J., A. Adcroft, C. Hill, L. Perelman, and C. Heisey, 1997a: A finite-volume, incompressible Navier Stokes model for, studies of the ocean on parallel computers. *J. Geophys. Res.*, **102** (C3), 5753–5766, doi:10.1029/96JC02775.
- , C. Hill, L. Perelman, and A. Adcroft, 1997b: Hydrostatic, quasi-hydrostatic, and nonhydrostatic ocean modeling. *J. Geophys. Res.*, **102** (C3), 5733–5752, doi:10.1029/96JC02776.
- Michalakes, J., J. Dudhia, D. Gill, T. Henderson, J. Klemp, W. Skamarock, and W. Wang, 2004: The Weather Research and Forecast Model: Software architecture and performance. *Proc. 11th Workshop on the Use of High Performance Computing in Meteorology*, Reading, United Kingdom, ECMWF, 156–168.
- Paeth, H., and M. Diederich, 2011: Postprocessing of simulated precipitation for impact research in West Africa. Part II: A weather generator for daily data. *Climate Dyn.*, **36**, 1337–1348, doi:10.1007/s00382-010-0840-0.
- Palazzi, E., J. von Hardenberg, and A. Provenzale, 2013: Precipitation in the Hindu-Kush Karakoram Himalaya: Observations and future scenarios. *J. Geophys. Res. Atmos.*, **118**, 85–100, doi:10.1029/2012JD018697.
- Rebora, N., L. Ferraris, J. von Hardenberg, and A. Provenzale, 2006a: Rainfall downscaling and flood forecasting: A case study in the Mediterranean area. *Nat. Hazards Earth Syst. Sci.*, **6**, 611–619, doi:10.5194/nhess-6-611-2006.
- , —, —, and —, 2006b: RainFARM: Rainfall downscaling by a filtered autoregressive model. *J. Hydrometeorol.*, **7**, 724–738, doi:10.1175/JHM517.1.
- Schreiber, T., and A. Schmitz, 1996: Improved surrogate data for nonlinearity tests. *Phys. Rev. Lett.*, **77**, 635–638, doi:10.1103/PhysRevLett.77.635.
- Solomon, S., D. Qin, M. Manning, Z. Chen, M. Marquis, K. Averyt, M. Tignor, and H. L. Miller Jr., Eds., 2007: *Climate Change 2007: The Physical Science Basis*. Cambridge University Press, 996 pp.
- Sorooshian, S., K. I. Hsu, E. Coppola, B. Tomassetti, M. Verdecchia, and G. Visconti, 2008: *Hydrological Modelling and the Water Cycle Coupling the Atmospheric and Hydrological Models*, Water Science and Technology Library, Vol. 63, Springer-Verlag, 138 pp.
- Uppala, S. M., and Coauthors, 2005: The ERA-40 Re-Analysis. *Quart. J. Roy. Meteor. Soc.*, **131**, 2961–3012, doi:10.1256/qj.04.176.
- von Hardenberg, J., L. Ferraris, N. Rebora, and A. Provenzale, 2007: Meteorological uncertainty and rainfall downscaling. *Nonlinear Processes Geophys.*, **14**, 193–199, doi:10.5194/npg-14-193-2007.
- Washington, W. M., and C. L. Parkinson, 2005: *An Introduction to Three-Dimensional Climate Modeling*. University Science Books, 353 pp.
- Wilby, R. L., and H. J. Fowler, 2010: Regional climate downscaling. *Modelling the Impact of Climate Change on Water Resources*, F. Fung, A. Lopez, and M. New, Eds., John Wiley and Sons, 34–85.